chemosensors

Article

Heater Topology Influence on the Functional Characteristics of Thin-Film Gas Sensors Made by MEMS-Silicon Technology

Gennady Gorokh [1,*], Igor Taratyn [2], Uladzimir Fiadosenka [1], Olga Reutskaya [2] and Andrei Lozovenko [1]

[1] R&D Laboratory of Nanotechnologies, Belarusian State University of Informatics and Radioelectronics, 220013 Minsk, Belarus; v.fedosenko@bsuir.by (U.F.); lozovenko.andrey@gmail.com (A.L.)
[2] Instrumentation Engineering Faculty, Micro- and Nanotechnology Department, Belarusian National Technical University, 220013 Minsk, Belarus; mnt@bntu.by (I.T.); oreutskaya@gmail.com (O.R.)
* Correspondence: gorokh@bsuir.by; Tel.: +375-29-3474903

Abstract: The design of the heater plays a decisive role in the energy consumption, sensitivity, and speed of chemical sensors. The paper analyzes various options for the topology of meander-type platinum heaters in chemical sensors fabricated on thin dielectric membranes using MEMS-silicon technology. Comprehensive studies of the heater's current–voltage characteristics have been carried out, heating rates have been measured at various currents, experimental temperature characteristics for various meander topologies have been obtained, heater options have been determined, and optimal heat transfer processes are ensured at a low power consumption of about 20–25 mW. Sensors with an optimal heater topology based on a double dielectric membrane were fabricated according to the described technological process, and sensory responses to 0.5 vol.% CH_4 and 0.2% C_3H_8 were studied. The obtained results showed good results and confirmed the need to choose the optimal heater topology when designing sensors for recording the given type of gas mixtures in a certain temperature range.

Keywords: chemical sensor; current–voltage characteristics; heater topology; MEMS-silicon technology; anodic alumina membrane

check for updates

Citation: Gorokh, G.; Taratyn, I.; Fiadosenka, U.; Reutskaya, O.; Lozovenko, A. Heater Topology Influence on the Functional Characteristics of Thin-Film Gas Sensors Made by MEMS-Silicon Technology. *Chemosensors* **2023**, *11*, 443. https://doi.org/10.3390/chemosensors11080443

Academic Editor: Bilge Saruhan-Brings

Received: 19 June 2023
Revised: 4 August 2023
Accepted: 7 August 2023
Published: 9 August 2023

1. Introduction

During gas sensor development for portable devices, considerable attention is paid to minimizing power consumption, high cross-selectivity and sensitivity of the active element, speed of response and regeneration, as well as reproducibility of measurements of sensor responses to low concentrations of controlled gases, service life, and reliability [1,2]. High selectivity is achieved by the purposeful selection of gas-sensitive materials based on metal oxides, by doping them with ions of other metals with appropriate alloying additives, and by comparing the physicochemical patterns of energy changes in surface adsorption centers [3,4]. One of the ways to increase the selectivity of gas-sensitive layers is the formation of semiconductor mixed metal oxides with a large effective surface, the grain size of which can be controllable varied [5,6], thus changing the electrical conductivity of such films in a certain temperature range, depending on the composition and state of the surface [7–9]. When n-type semiconductor metal oxides interact with oxidizing gases, oxygen ions are adsorbed on the film surface (including hydroxyl groups OH–), the conduction band is depleted of electrons, and the potential barrier and resistance of the metal oxide film increases. When n-type semiconductors interact with reducing gases, the oxidation reaction of gas molecules occurs under interaction with ion-sorbed oxygen, which leads to the enrichment of the conduction band of the semiconductor with electrons, decreasing in the potential barrier and, as a result, to decrease in the resistance of the metal oxide film [10–12].

The sensitivity to a particular gas is associated with changes in the properties of the material during the course of the adsorption reaction and depends on the temperature of

the gas-sensitive material [13,14]. The sensitivity of sensors can be increased by using a nanostructured gas-sensitive layer [15–18], which has an increased effective area of interaction between metal oxides and gas medium molecules. One of the options for structuring metal oxide films is the deposition of gas-sensitive films on highly ordered nanoporous matrices of anodic alumina (AA), as a result of which it is possible to increase the sensitivity of the films [19–23]. The crystallization of condensed films in pores ensures the homogeneity of the formed grains, and the granularity facilitates the access of gas molecules deep into the gas-sensitive layer and increases the efficiency of reactions occurring on the nanostructured surface [24–28].

The diminution of the sensor energy consumption is ensured by reducing the size of the gas-sensitive layer heating area and reducing losses during heat dissipation, which is achieved by the design features of the sensor, localization of the heating area, and reducing the mass (area and thickness) of the gas-sensitive layer. [29–31]. The most energy-consuming part of the chemical sensor is the sensitive element since the sensor needs to be heated to temperatures in the range of 150–500 °C, depending on the type of gas being detected [32,33].

In the process of optimizing the characteristics, the improvement in one sensor parameter leads to the deterioration of another; depending on the purpose of the sensor device, it is necessary to sort out different options for its design and the sequence of technological route operations, the sensitive layer materials composition, temperature conditions, etc. [34,35]. At the same time, by analyzing the above, we can conclude that with all the optimized parameters, the effective operation of modern sensors is possible only with a controlled temperature regime in a given range provided by a properly selected thin-film heater.

The paper considers various design options for sensors with different topologies of a meander-type heater, in which optimal heat exchange processes are ensured with low power consumption, and the main characteristics of thin-film sensors with such heaters manufactured by MEMS-silicon technology using nanostructured gas-sensitive thin films on anodic alumina membranes are studied [36–38].

2. Design and Manufacturing Technology of the Studied Thin-Film Sensors

2.1. Sensor Designs with Different Heater Topologies

To study heat transfer processes in sensors with different topologies of heaters, we used thin-film sensors on dielectric membranes in silicon wafers manufactured using MEMS—silicon technology [39,40]. The sensor design itself was a Si substrate with an area of 1.35 × 1.35 mm and a thickness of 0.38 mm, in the center of which a dielectric membrane 500 × 500 × 1.2 μm in size was formed, consisting of a layer of unstressed Si_xN_y 0.3 μm thick and AA layer 0.9 μm thick. A platinum heater and a sensitive layer were located on the flat side of the double dielectric membrane on the surface of the AA. The thickness of the platinum layer was 200 nm. The heating elements are made in the form of meanders but have different topologies and resistor lengths. The nanoporous structure of AA, which is a periodic matrix of parallel hexagonal symmetry cells with central cylindrical pores, improves their mechanical properties, namely elasticity, hardness, wear resistance, etc. [41,42]. This makes it possible to use it in the design of chemical sensors as both a directly passive dielectric substrate, on which the structural elements of chemical sensors are placed, and a regular nanostructured matrix, on which the sensitive layer is formed by filling the pores with a certain material. It is important to note that the dimensions of the cell itself and the diameter of the AA pore can vary within the wide range, which makes it possible to purposefully control the characteristics of chemical sensors by optimizing the structural parameters and properties of the AA.

The schematic representation of the sensor design with the meander-shaped heater located on the double dielectric membrane in a window in silicon platinum is shown in Figure 1. The basic topology of the heater is a six-loop meander 460 μm long and 200 μm wide with a conductor width of 30 μm and a gap between the conductors of 5 μm. There are external contacts sized 295 × 295 μm at the ends of the heater. The general view of

the topology of the first type of heater with geometric dimensions is shown in Figure 2a. The second topology of the heater is the meander of the first type divided along the axial line into two parts. Such topology allows the connection of the heater to two halves in series or in parallel, providing different currents and, consequently, temperature modes of its operation. The appearance and geometric dimensions of the second type of heater are shown in Figure 2b. The heater's third type is half of the basic meander or one-half of the heater's second type. All the topological dimensions of the conductors were retained, but the heater resistor length and its area were halved (Figure 2c).

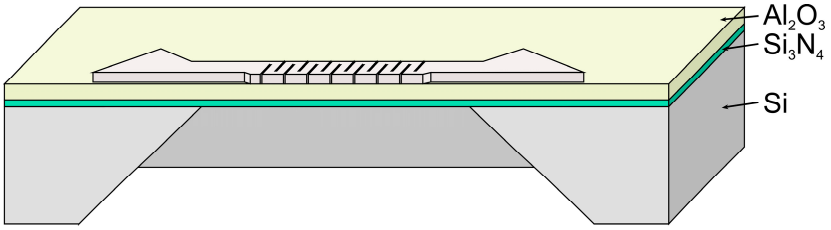

Figure 1. Schematic representation of the construction of platinum heater for the thin-film sensor on double dielectric Si_xN_y/AOA membrane in a locally etched window in a silicon wafer.

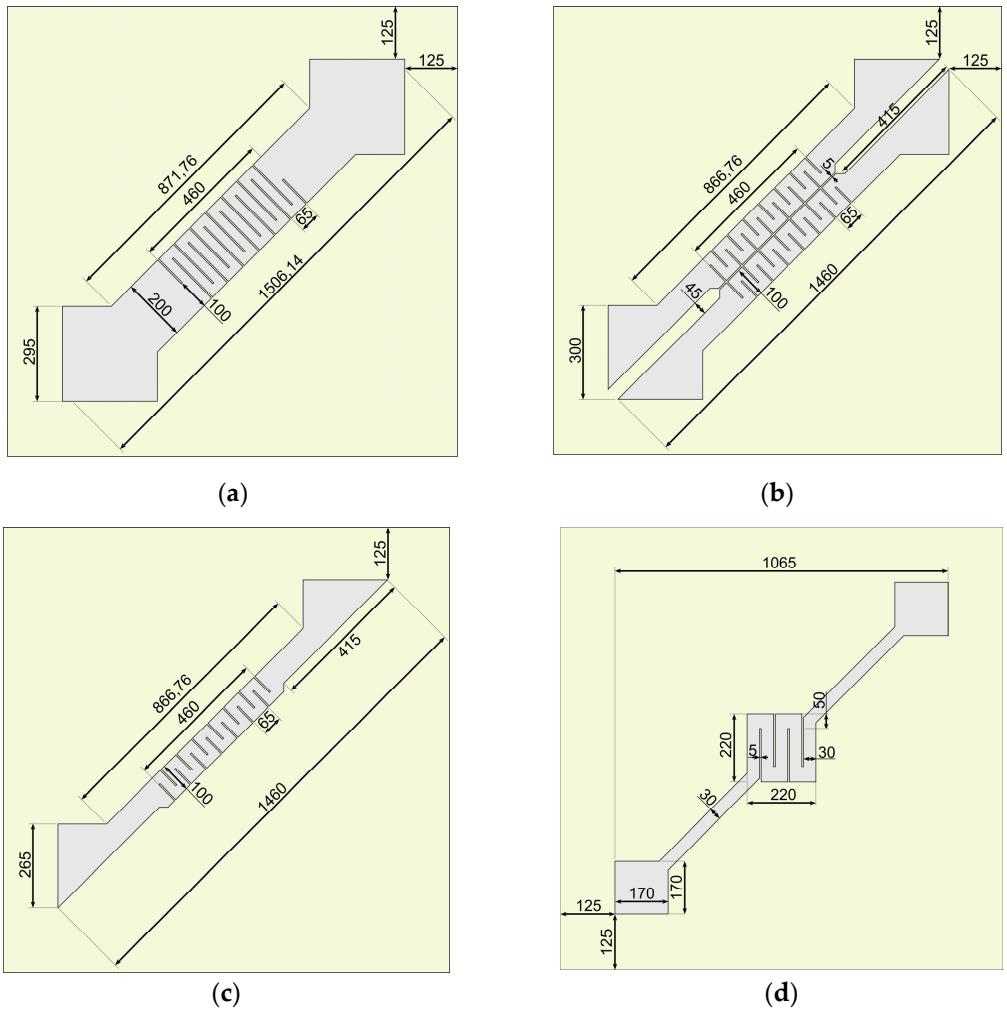

Figure 2. Different options for the topology of the sensor heater on a two-layer Si_xN_y/Al_2O_3 membrane: (**a**)—big six-loop meander with conductor **1t**; (**b**)—serial connection of two halves of first type heater **2t**; parallel connection of two halves of first type heater **3t**; (**c**)—half of the first meander **4t**; (**d**)—small square two-loop meander **5t**.

The fourth version of the heater topology significantly differs from the three previous ones both in the shape of the meander and its dimensions, with the same values of the width of the conductors and the gaps between them, which corresponds to 30 μm and 5 μm. The meander size is 220 × 220 μm, and its area corresponds to half the area of the base meander (Figure 2d).

2.2. Technological Process of Manufacturing Thin-Film Sensors

2.2.1. Creation of Double Dielectric Membrane in Silicon Substrate

The manufacturing route for thin-film sensors on a double dielectric membrane consisted of three technological processes: the creation of a thin membrane in a silicon wafer, the formation of a heater, and the deposition of a gas-sensitive layer. To form a thin double dielectric membrane, a p-type silicon wafer (<100>) was used, which was pretreated in a hot ammonium peroxide solution, washed, and dried (Figure 3a). Then, a layer of unstressed silicon nitride Si_xN_y was deposited onto the substrate (Figure 3b) using a SemiTeq STEISPd81L setup, and double-sided photolithography was performed to mask the front side of the substrate and form a pattern of windows for membranes on the reverse side of the substrate (Figure 3c). Next, Si_xN_y was removed in the windows from the reverse side of the substrate to the Si surface (Figure 3d) and deep anisotropic alkaline etching of silicon (Figure 3e), leaving a silicon layer about 100 μm thick. After removing the photoresist (Figure 3f), the layer of aluminum 1.5 μm thick was deposited on the front side of the substrate (Figure 3g), and AA film 0.8 μm thick was formed on the Si_xN_y surface using the two-stage anodization [43] in the potentiostatic mode at Ea = 50 V in oxalic acid solution (Figure 3h). The electrical anodization modes were set using a Keysight N5751A system DC power supply, and the process parameters were recorded and monitored in situ using a Keysight 34470A digital multimeter connected via USB to a personal computer with the installed Bench Vue software.

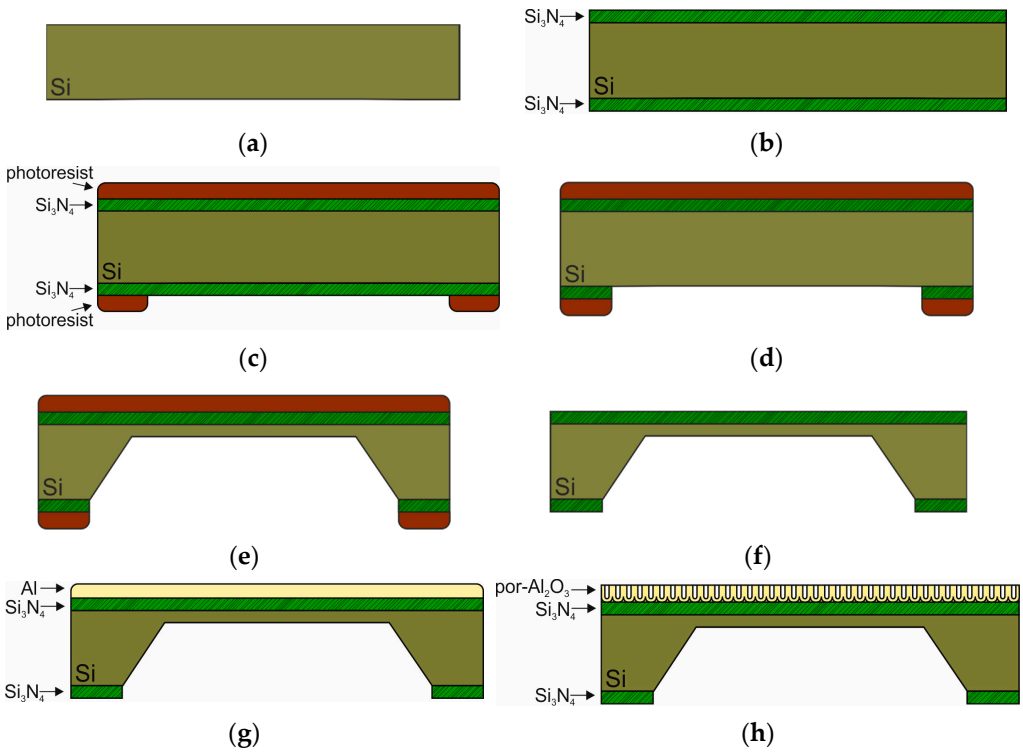

Figure 3. Stages of formation of a two-layer membrane on a silicon substrate: (**a**)—Si substrate cleaning; (**b**)—plasma-chemical deposition of Si_xN_y; (**c**)—photolithography on the windows pattern; (**d**)—plasma-chemical etching of Si_xN_y; (**e**)—anisotropic Si etching; (**f**)—photoresist removal; (**g**)—Al sputtering; (**h**)—two-stage electrochemical Al anodizing.

Figure 4 shows micrographs of the formed window in the silicon substrate from the reverse side (Figure 4a), the cross-section of this window with the membrane (Figure 4b), and the cross-section of the double dielectric membrane (Figure 4) obtained using scanning electron microscope Hitachi S-806.

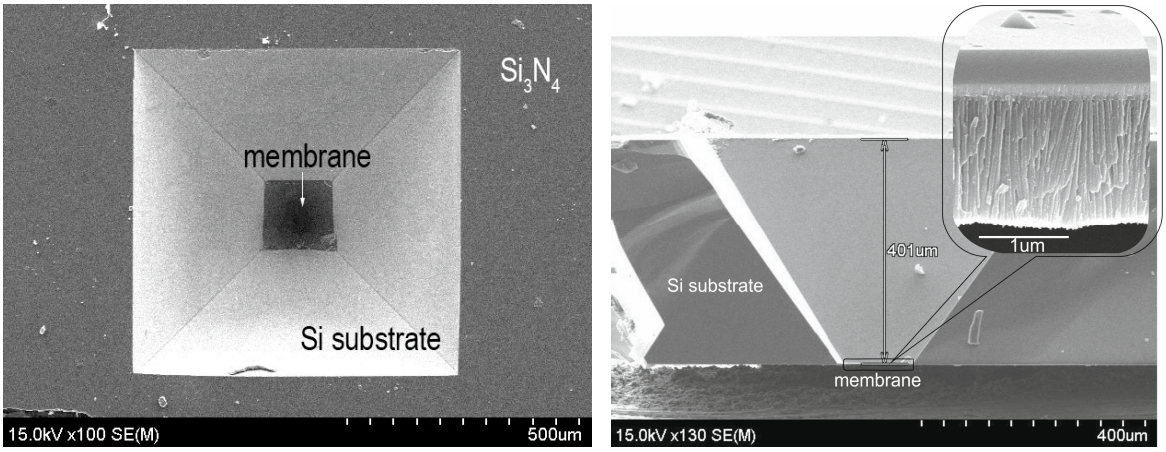

(**a**) (**b**)

Figure 4. A window with a double dielectric SixNy/AOA membrane in a silicon substrate formed by local anisotropic etching: (**a**)—view of the window from the back of the substrate; (**b**)—substrate cross-section in the window area; (insert (**b**))—cross-section of double dielectric membrane Si_xN_y/AA.

2.2.2. Fabrication of the Heater on Double Dielectric Membrane

Platinum films with high electrical conductivity and thermal stability were used as the microheater material [44]. The use of the AA layer in dielectric membranes makes it possible to solve the problem of platinum adhesion to silicon and silicon nitride; on the relief surface of the AA, Pt films have good adhesion. The Pt layer deposition on a two-layer dielectric membrane was carried out using magnetron sputtering using an Edwards ESM100 vacuum setup at operating power W = 100 W and pressure in the working chamber $p = 5 \times 10^3$ mbar. Figure 5 shows electron microscopic images of the AA membrane surface (Figure 5a) and the surface of 200 nm thick deposited Pt on it (Figure 5b). Platinum uniformly fills the pores of the AA while the entrances to the pores remain open, which makes it possible to subsequently form structured active layers on top of the microheater. The schematic representation of the technological operations sequence for the formation of the heater and electrodes on the dielectric membrane in the silicon substrate is shown in Figure 6.

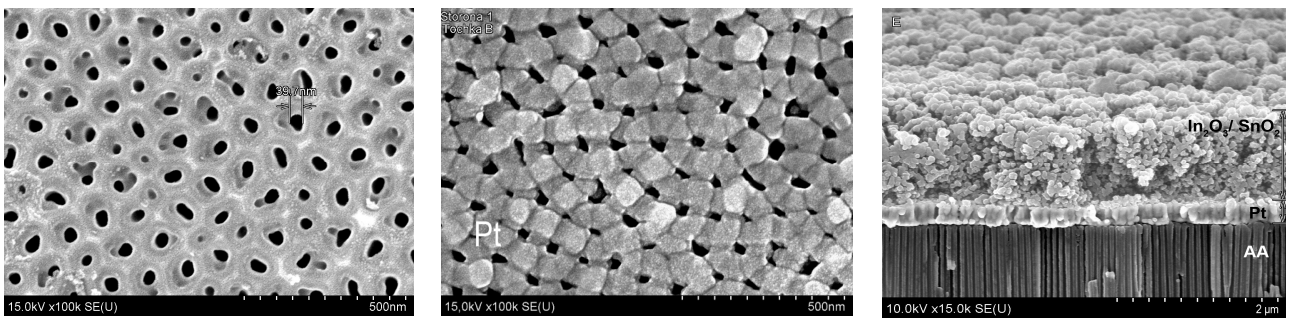

(**a**) (**b**) (**c**)

Figure 5. SEM images: (**a**)—the surface of AA membrane; (**b**)—the surface of deposited Pt on AA membrane; (**c**)—cross-section of AA membrane with the gas-sensitive layer of In_2O_3-SnO_2 deposited on the platinum heater.

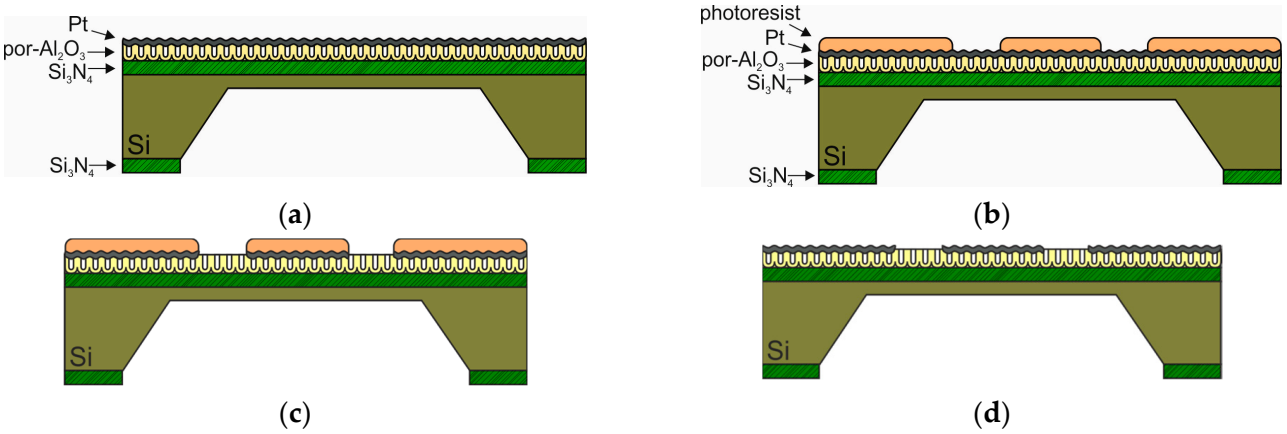

Figure 6. Stages of forming a heater and electrodes on a nanoporous dielectric membrane in a silicon substrate: (**a**)—sputtering Pt; (**b**)—photolithography based on the heater and electrodes pattern; (**c**)—plasma-chemical etching of Pt; (**d**)—photoresist removal.

The photoresist was applied to the Pt layer deposited on the two-layer dielectric membrane (Figure 6a), and photolithography was carried out according to the pattern of the microheater and control electrodes (Figure 6b). Then, the platinum film was etched using plasma-chemical etching in the C_3F_8/N_2 atmosphere to form the topology of the heater and electrodes according to the pattern (Figure 6c) and remove the photoresistive mask (Figure 6d).

2.2.3. Deposition of Gas-Sensitive Layer

Before the deposition of the gas-sensitive layers on nanoporous membranes, an operation was performed to remove the non-etched silicon layer left in the windows to provide the necessary rigidity of the membranes during the formation of the heater and electrodes. To prevent clogging of AA pores during masking, a vanadium layer was deposited on the front side of the membrane. (Figure 7a). Next, the samples were covered with a layer of paraffin, on which a silicon plate was glued to provide the necessary rigidity of the membrane when silicon was etched (Figure 7b), and local anisotropic silicon was etched into the membrane surface in a 35% KOH solution at a temperature of 80 °C. (Figure 7c). After that, the paraffin was melted in a water bath, the satellite plate was removed (Figure 7d), and the masking layer of vanadium was dissolved using cyclic treatment in 30% H_2O_2 and H_2O at intervals of t = 30 s (Figure 7e). Next, an active layer was applied to the surface of the heater using ion layering (drip deposition) from aqueous solutions or sol-gel deposition in such a way that it closed the ends of the signal electrodes (Figure 7f).

The most common metal oxides used as a sensitive layer for detecting a large number of gases, such as O_2, H_2, CO, CO_2, NO, NO_2, CH_4, NH_3, H_2S, etc., is tin oxide—SnO_2. At the same time, this is the main disadvantage, which consists of the difficulty of separating signals from different gas mixtures [20,21]. In_2O_3 films are also widely used in gas sensors, but their electrical parameters differ significantly from those of SnO_2 [20–22,45]. The combination of these two materials retains the merits of both while smoothing out problematic issues in their use, including minimizing resistivity [46]. However, obtaining In_2O_3-SnO_2 films of the required composition using plasma physicochemical deposition methods is associated with certain difficulties, consisting of a significant difference between the evaporation temperatures of indium and tin compounds, as well as the need to provide different evaporation rates. For this reason, the sol-gel method is the most convenient for obtaining films of a given composition.

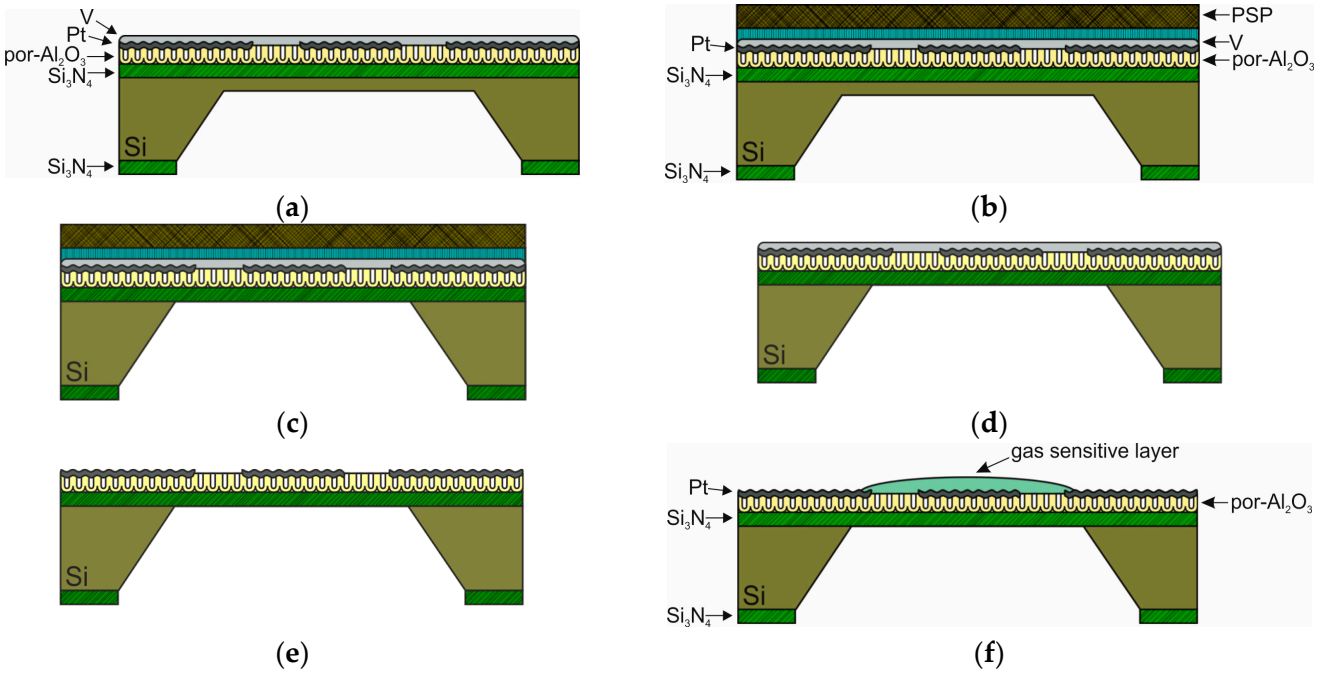

Figure 7. Stages of membrane preparation and application of the active layer: (**a**)—spraying of V; (**b**)—masking of the front side of the membrane with paraffin and silicon plate (PSP); (**c**)—local anisotropic additional etching of Si in windows; (**d**)—removal of paraffin and satellite plate; (**e**)—dissolution of V; (**f**)—application of the active layer.

Sols of indium and tin hydroxides were obtained by dissolving 10 g of $SnCl_4$ in 20 mL of deionized water and 15 g of $In(NO_3)_3$ in 20 mL of deionized water. The solutions were mixed, and the resulting composition was intensively stirred until complete dissolution and a homogeneous solution was obtained, centrifuged, and dispersed using ultrasound. To obtain a gel, a few drops of 50% NH_4OH, which is also a stabilizer of the colloidal state, were added to the solution of $In(OH)_3$ and $SnO_{2-x}(OH)_{2x}$ [35]. The solution with precipitated gel was kept for 2–3 h, purified using centrifugation, and placed in an ultrasonic bath for 1 h. The gel was applied in doses of 2 µL to the hot heater surface when a current was applied to the electrodes. Each deposited layer was dried at 70 °C (I = 16 mA) for 15 s and annealed at 600 °C (I = 35 mA) for 15 s, turning the temperature up to 600 °C for 20 s. To obtain uniform gas-sensitive films of sufficient thickness (about 2–3 µm), up to 10 gel layers were applied. Figure 5c shows the cross-section of the AA membrane with the gas-sensitive layer of In_2O_3-SnO_2 deposited on the platinum heater.

To study heat transfer processes in sensors with different heater topologies, thin-film systems were fabricated using the MEMS-silicon technology of four design options using the described technological route.

3. Influence of the Sensor Heater Topology on Heat Exchange Processes

3.1. Investigation of Current–Voltage Characteristics of Heaters with Different Topologies

The influence of the heater topology on the electrical and temperature characteristics of the sensors was carried out on sensor structures fabricated according to the described technological process without deposition of the gas-sensitive layer. For the convenience of comparing the electrical and temperature characteristics of sensors with different heater topologies, each sensor was given the conventional name:

- First topology (**1t**)—big six-loop meander with conductor width of 30 µm and gap between them of 5 µm (Figure 2a);
- Second topology (**2t**)—serial connection of two halves of the first type heater, divided along the axis (Figure 2b);

- Third topology (**3t**)—parallel connection of two halves of the first type heater, divided along the axis (Figure 2b);
- Fourth topology (**4t**)—half of the first meander (Figure 2c);
- Fifth topology (**5t**)—small square two-loop meander (Figure 2d).

Table 1 shows the main geometric parameters of the topologies of the studied sensors.

Table 1. The main topologies parameters of the studied sensors.

Title Topology	Heater Area, mm^2	Conductor Length, mm	Conductors Squares Number	Heater Resistance, Ohm
1t	0.092	2.4	84	12.18
2t	0.092	2.6	100	13.82
3t	0.092	1.3	50	3.51
4t	0.046	1.3	51.5	7.24
5t	0.0484	1.1	37 + 22	10.15

Comparing the topologies of different heaters (Table 1), it should be noted that the first three heater options have the same area of 0.092 mm^2 with approximately the same length of the resistive conductor, 2.4–2.6 mm. The area of the fourth and fifth types of heaters is two times smaller, and it is 0.046 mm^2 with a shorter conductor length of 1.1–1.3 mm. The resistance of the heaters correlates with the length of the platinum conductors. To estimate the resistance of the heater conductor, we calculated the number of squares in the conductors of different topologies, including the external conductors leading to the heater. In topology **5t**, the length of the heater conductor is 37 squares, and the electrodes leading to it are 22 squares, that is, more than half the length of the heater conductor. Table 1 also shows the resistance values of these heaters.

The rate and uniformity of sensors heating with different types of heater topology were evaluated by measuring the current–voltage characteristics (CVC) when a current was passed through the heaters, increasing in 10 mA increments. All electrical measurements were performed using the set of measuring instruments from Keysight: electrical modes were set using a Keysight B2901A parametric analyzer, and currents and voltages were recorded using a Keithley 6485 ammeter and Keysight 34470A multimeter. All data were digitally transferred to a computer via the USB interface in the EasyEXPERT group+ software environment. In the process of the research, CVCs were automatically plotted on the monitor screen. The temperature of the heaters was recorded using a non-contact method within the range of 20–700 °C using a stationary high-precision digital infrared pyrometer IMPAC IPE 140 (LumaSense, Frankfurt/Main, Germany) with a spectral range of 3.9 μm. In addition, the degree of heating of the heater was qualitatively assessed by visually recording the spectral changes during the heating of the working area from dark red (DR) to bright red (BR) glow and the values of the currents at which the glow appeared, as well as the dissipated power on the heater, were recorded.

Figure 8 shows the measured CVCs of the sensors under study, indicating the temperatures of the heaters in certain electrical modes. Figure 8a shows the CVC for the first type of heater topology shown in Figure 2a. It is characterized using a significant nonlinearity, a narrow current range, at which the central part of the heating region changes color from DR (35 mA) to BR (41 mA), and low heating power to DR color of about 37.5 mW.

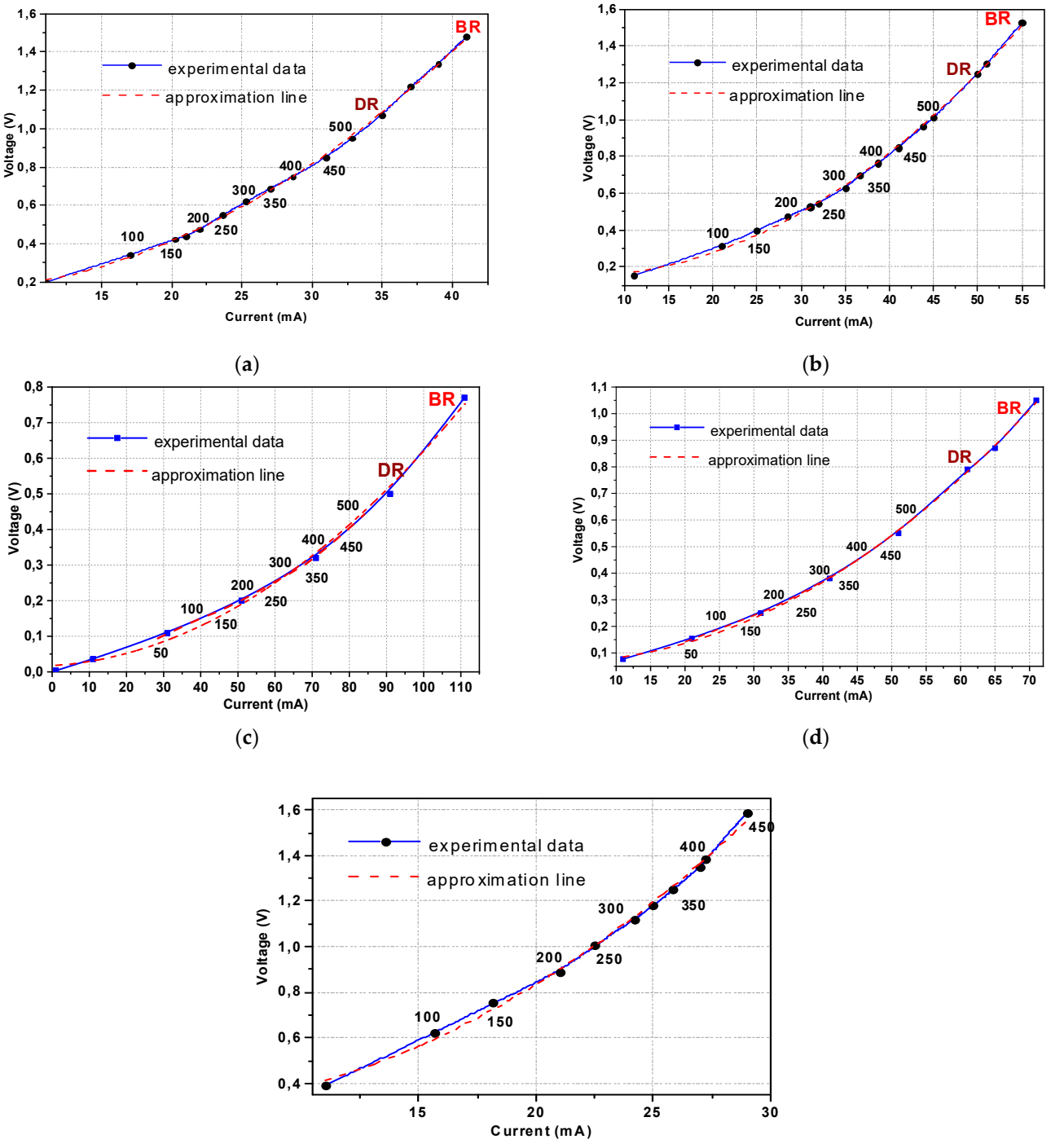

Figure 8. Sensors CVCs with different heaters topology: (**a**)—big six-loop meander with conductor **1t**; (**b**)—serial connection of two halves of first type heater **2t**; (**c**)—parallel connection of two halves of first type heater **3t**; (**d**)—half of the first meander **4t**; (**e**)—small square two-loop meander **5t**.

The CVC of the heater, which is the series connection of two halves of the first type heater (Figure 8b), also has significant nonlinearity and a small range of color change currents from **DR** to **BR** (50–55 mA), but higher heating power (62.5–83.5 mW) to red. When the two halves of the heater of the second type are connected in parallel, its CVC is the closest to linear dependence (Figure 8c). In addition, it should be noted that when this type of heater is switched on this way, the **DR** area appears already at a current of

92 mA, which corresponds to power of 48.3 mW and **BR**—at 110 mA. Thus, the wider range of temperature control of the sensor working area is observed by changing the value of the heating current from 70 to 110 mA. The fourth heater topology CVC, which is half of the base heater, has less linear dependence compared to the double heater connected in parallel but smoother than that of the first and second types connected in series (Figure 8d). The **DR** glow appears at 60 mA, which corresponds to a power of 46 mW, and quickly turns into **BR** already at 70 mA; that is, the heating control current range is only 10 mA. The heater CVC manufactured according to the fifth topology (Figure 8e) also has good linearity, but this topology is characterized by small current ranges for heating the sensors to the specified operating temperatures. For this reason, the glow on the heater was not recorded.

3.2. Study of Heater Temperature Dependences with Different Topologies

Analyzing the CVCs of the studied sensors, it can be noted that the values of the power dissipated at maximum heating until the appearance of **DR** and **BR** glow do not correlate with the geometric dimensions of the heaters. **DR** glow appears initially in the central part for all types of heaters at a temperature of about 620–650 °C. Here, power dissipation, sensor housing design, and assembly technology have a significant impact. The temperature at which **BR** glow appears lies in the range of 780–820 °C for different types of heaters. From the point of view of controlling the heater temperature in wide-range currents, the topology of the second type is most preferable when two halves are connected in parallel, while **DR** glow appears in this design at relatively low power. In addition, the large area of the heater ensures uniform heating of the active layer of the sensor. Low power is spent on heating the heater to **DR** glow in the heater of the fifth type, and minimum power is required for the appearance of **BR** glow in such a sensor, but the small current range of about 4 mA does not allow high accuracy to control the heater temperature. These considerations are valid for the high-temperature region, but since the sensors, depending on the analyzed gases and the gas-sensitive materials used, operate in narrow temperature ranges within the temperature range from 100 to 500 °C, different topologies can have temperature features in the operating ranges. However, the main thing is minimizing power consumption with high and stable indicators of sensitivity and speed.

Figure 9 shows the temperature dependences on the dissipated power in the heaters under study. The maximum power expended on heating to certain temperatures is expended in the heater **5t**—the small square meander with narrow supply electrodes. So, for example, for heating up to 100 °C, the **5t** heater needs to spend 9.75 mW, while in the large **1t** meander or in one half of the large meander, a little more than 4.85 and 5.75, respectively.

This proportion of energy consumed is maintained when heated to 200–500 °C. Increased energy costs are observed at the **2t** heater—two halves of meander connected in series, which needs 6.6 mW to heat up to 100 °C, 22 mW to 300 °C, and up to 500 °C—42 mW. Comparatively lower losses are for the heater **3t**—two halves of the meander connected in parallel. The minimum power consumption in all temperature ranges is provided by the heater with the first topology **1t**—the large meander, and the half meander **4t**. At the same time, at temperatures up to 300 °C, the energy consumption of **1t** is lower, and to achieve higher temperatures, heaters **1t** and **4t** require almost the same power.

3.3. Study of Gas-Sensing Properties of Investigated Sensors

Figure 10a shows the dependences of the temperature on the heaters under study on the magnitude of the current, from which it can be seen that the maximum heating rate for heaters is **1t** and **5t**, but for heating up to 450 °C, power of 42.75 mW must be applied to the heater **5t**, and for **1t**—only 26.35 mW. The same graph highlights the temperature ranges that are most preferable for recording different types of gases, including for the In_2O_3-SnO_2 films we use. To measure the gas-sensing properties of sensors, a **1t** heater was chosen from the set of topologies under study, which provides fast and uniform heating at low power consumption and operates stably at high temperatures. The response of such sensors to

CH_4 and C_3H_8 was studied on an experimental bench consisting of a measuring cell, a system for creating and maintaining a given gaseous medium in the cell, and devices for measuring electrical signals. All the electrical measurements were performed using the set of measuring instruments from Keysight described above. As calibration gas mixture was used CH_4–0.5 vol.% and C_3H_8–0.2 vol.% diluted in purified air ($2O_2 + N_2$). The measurements were carried out in the measuring cell at room temperature (20–25 °C) and humidity maintained using a humidity generator in the range of 40–45%. The control over the course of the experiment was carried out using information recorded using measuring instruments and the gas flow microcontrollers of the gas generator, transmitted to the personal computer. The measurement cycle began with switching on the gas generator valves in combination, providing the minimum content of the initial gas in the gas mixture (CH_4–0.5 vol.%), after which the gas mixture, after preliminary pumping, was fed into the measuring cell. The measurements were carried out at a set current on the **1t** topology heater, which provided the optimal temperature for recording this gas. The sensor sensitivity was determined as the ratio of the sensor resistance in air (R_{air}) to the sensor resistance when exposed to active gas (Rgas): $S = R_{air}/R_{gas}$.

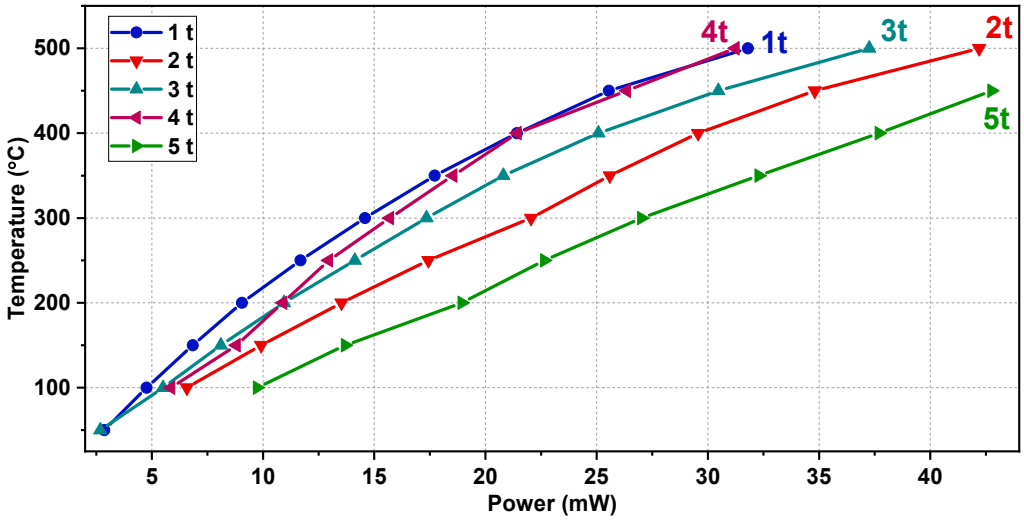

Figure 9. Dependences of temperature on the Energy consumption for heaters with different topologies are shown in Figure 2: (**1t**)—big six-loop meander with conductor; (**2t**)—serial connection of two halves of first type heater; (**3t**)—parallel connection of two halves of first type heater; (**4t**)—half of the first meander; (**5t**)—small square two-loop meander.

Figure 10b shows the responses of the sensors with **1t** topology at a current of 30 mA for 0.5 vol% CH_4 and at a current of 27 mA for 0.2 vol% C_3H_8. These responses to methane and propane showed good sensitivity. For 0.2% C_3H_8, the sensor sensitivity was 1.279 at a gas-sensitive layer temperature of 350 °C, while the power dissipation on the heater was 17.7 mW at a heating current of 27 mA. For 0.5 vol.% CH_4 at a heating current of 30 mA (23.9 mW, 430 °C), the sensor sensitivity was 1.222.

The fabricated sensors showed the long-lasting stability of heaters on the anodic alumina thin-film membrane. Changes in heater resistance after 100 h of continuous operation averaged less than 1%. At the same time, the stability of the heater, made according to the first topology, was less than 0.5% at a temperature of 150 °C and less than 1.5% at a temperature of 450 °C (current 31 mA) after 250 h of operation. These heater parameters provide stable and reproducible sensor parameters when measuring methane and propane (Figure 10b) at the level of 2.5%. The long-lasting stability corresponds to the high rates of such systems. Since not only the heater but also the overall long-lasting effect of the gas-sensitive material affects the stability of the sensor stability and its deposition method, this value corresponds to the high characteristics of the stable operation of such a system [47].

Thus, the conducted studies confirmed the assumptions about the need to choose the correct topology of the heater when designing sensors for registering particular gas, providing optimal temperature and functional characteristics—power consumption and sensitivity to the limiting concentrations of gas mixtures.

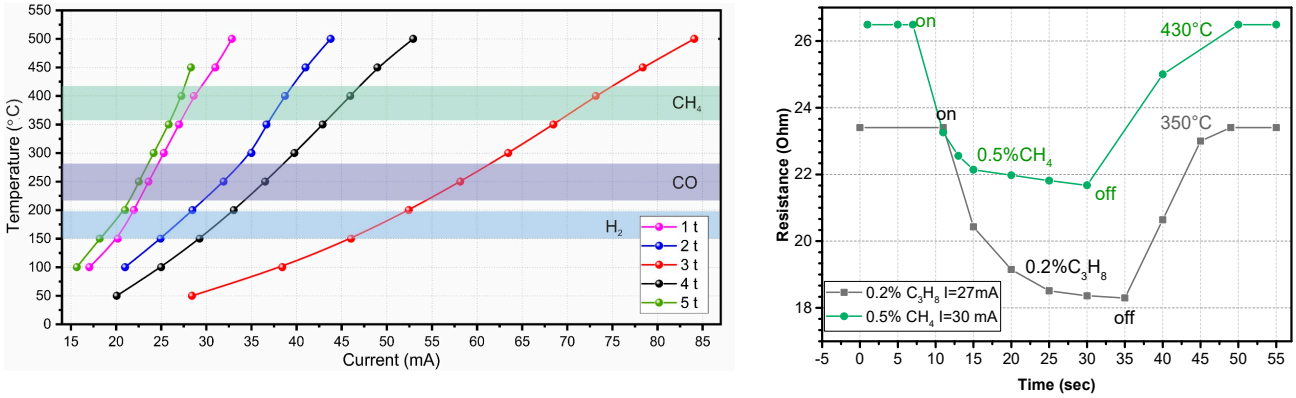

(**a**) (**b**)

Figure 10. (**a**)—Dependences of temperature on heating current for different heater topologies shown in Figure 2: (**1t**)—big six-loop meander with conductor; (**2t**)—serial connection of two halves of first type heater; (**3t**)—parallel connection of two halves of first type heater; (**4t**)—half of the first meander; (**5t**)—small square two-loop meander. (**b**)—The responses of the sensor with **1t** topology at a current of 30 mA for 0.5 vol% CH_4 and at a current of 27 mA for 0.2 vol% C_3H_8.

4. Conclusions

The results of a comprehensive analysis of the functional characteristics of chemoresistive sensors with meander-type platinum heaters of various topologies are presented in this article. The heaters are placed on a double dielectric membrane of unstrained silicon nitride and nanoporous anodic aluminum oxide, locally located in a window formed using MEMS silicon technology by anisotropic silicon etching. Thanks to this design and the developed original technology, it was possible to achieve a fundamental reduction in power consumption during rapid heating to operating temperatures reaching 450–500 °C. An analysis was made of the influence of the heater topology in sensors of this design on their electrical (controlled current and voltage control) and thermal (heating rate and temperature distribution) characteristics, taking into account sensitivity, speed, and minimum power consumption in different temperature ranges depending on the type of the registered gas. The presented data show that when developing gas sensors for various purposes, it is necessary to take into account the features of heat exchange processes in heaters with minimal power consumption in order to control the temperature regime in a given range provided by a properly selected thin-film heater. Comparing four types of heater topologies for the sensor designed to detect gases in the region of elevated temperatures, the most preferable is the six-loop large meander, which provides heating control in the wide current range and fast heating to the dark red glow at the relatively low power, and the large heater area creates uniform heating of the sensor active layer. Studies of the sensor gas-sensitive characteristics with this heater topology showed a good sensitivity of 1.279 to 0.2% propane at 350 °C, which corresponded to the power consumption of 17.7 mW at a current of 27 mA. The sensitivity of the sensor to 0.5% methane was 1.222 at a current of 30 mA and power consumption of 23.9 mW. Choosing the right heater topology while registering the particular gas ensures optimal temperature and functional characteristics of the sensor—power consumption and sensitivity to low concentrations of gas mixtures.

Author Contributions: Conceptualization and writing—original draft preparation, G.G. Furthermore, U.F.; methodology, formal analysis, I.T. Furthermore, O.R.; data curation, investigation, validation, A.L. Furthermore, U.F.; writing—review and editing, G.G. Furthermore, I.T. All authors have read and agreed to the published version of the manuscript.

Funding: This research was carried out with the partial support of the State Research Program of the Republic of Belarus, "Micro- and Nanoelectronics", assignment 3.4.02.

Institutional Review Board Statement: Not applicable.

Informed Consent Statement: Not applicable.

Data Availability Statement: Not applicable.

Conflicts of Interest: The authors declare no conflict of interest. The funders had no role in the design of the study, in the collection, analyses, or interpretation of data, in the writing of the manuscript, or in the decision to publish the results.

References

1. Liu, X.; Cheng, S.; Liu, H.; Hu, S.; Zhang, D.; Ning, H. A Survey on Gas Sensing Technology. *Sensors* **2012**, *12*, 9635–9665. [CrossRef]
2. Kolmakov, A. Some Recent Trends in the Fabrication, Functionalisation and Characterisation of Metal Oxide Nanowire Gas Sensors. *Int. J. Nanotechnol.* **2008**, *5*, 450–474. [CrossRef]
3. Tang, H.; Yan, M.; Zhang, H.; Li, S.; Ma, X.; Wang, M.; Yang, D. A Selective NH_3 Gas Sensor Based on Fe_2O_3–ZnO Nanocomposites at Room Temperature. *Sens. Actuators B Chem.* **2006**, *114*, 910–915. [CrossRef]
4. Mondal, B.; Basumatari, B.; Das, J.; Roychaudhury, C.; Saha, H.; Mukherjee, N. ZnO–SnO_2 Based Composite Type Gas Sensor for Selective Hydrogen Sensing. *Sens. Actuators B Chem.* **2014**, *194*, 389–396. [CrossRef]
5. Fleming, W.J. New Automotive Sensors—A Review. *IEEE Sens. J.* **2008**, *8*, 1900–1921. [CrossRef]
6. Sharma, S.; Madou, M. A new approach to gas sensing with nanotechnology. *Philos. Trans. R. Soc. A* **2012**, *370*, 2448–2473. [CrossRef] [PubMed]
7. Comini, E.; Baratto, C.; Faglia, G.; Ferroni, M.; Vomiero, A.; Sberveglieri, G. Quasi-One Dimensional Metal Oxide Semiconductors: Preparation, Characterization and Application as Chemical Sensors. *Prog. Mater. Sci.* **2009**, *54*, 1–67. [CrossRef]
8. Carpenter, M.A.; Mathur, S.; Kolmakov, A. (Eds.) *Metal Oxide Nanomaterials for Chemical Sensors*; Springer: New York, NY, USA, 2013; ISBN 978-1-4614-5394-9.
9. Korotcenkov, G. Current Trends in Nanomaterials for Metal Oxide-Based Conductometric Gas Sensors: Advantages and Limitations. Part 1: 1D and 2D Nanostructures. *Nanomaterials* **2020**, *10*, 1392. [CrossRef]
10. Korotcenkov, G. Metal Oxides for Solid-State Gas Sensors: What Determines Our Choice? *Mater. Sci. Eng. B* **2007**, *139*, 1–23. [CrossRef]
11. Rajkumar, K.; Rt, R. Gas Sensors Based on Two-Dimensional Materials and Its Mechanisms. In *Fundamentals and Sensing Applications of 2D Materials*; Woodhead Publishing: Sawston, UK, 2019; pp. 205–258. ISBN 978-0-08-102577-2.
12. Barsan, N.; Weimar, U. Conduction Model of Metal Oxide Gas Sensors. *J. Electroceram.* **2001**, *7*, 143–167. [CrossRef]
13. Xu, C.; Tamaki, J.; Miura, N.; Yamazoe, N. Grain Size Effects on Gas Sensitivity of Porous SnO_2-Based Elements. *Sens. Actuators B Chem.* **1991**, *3*, 147–155. [CrossRef]
14. Moos, R.; Sahner, K.; Fleischer, M.; Guth, U.; Barsan, N.; Weimar, U. Solid state gas sensor research in Germany—A status report. *Sensors.* **2009**, *9*, 4323–4365. [CrossRef]
15. Chen, M.; Wang, Z.; Han, D.; Gu, F.; Guo, G. Porous ZnO Polygonal Nanoflakes: Synthesis, Use in High-Sensitivity NO2 Gas Sensor, and Proposed Mechanism of Gas Sensing. *J. Phys. Chem. C* **2011**, *115*, 12763–12773. [CrossRef]
16. Sik Choi, M.; Young Kim, M.; Mirzaei, A.; Kim, H.S.; Kim, S.I.; Baek, S.H.; Won Chun, D.; Jin, C.; Hyoung Lee, K. Selective, Sensitive, and Stable NO_2 Gas Sensor Based on Porous ZnO Nanosheets. *Appl. Surf. Sci.* **2021**, *568*, 150910. [CrossRef]
17. Yan, W.; Chen, Y.; Zeng, X.; Wu, G.; Jiang, W.; Wei, D.; Ling, M.; Wei Ng, K.; Qin, Y. Ultrasensitive ethanol sensor based on segregated ZnO-In_2O_3 porous nanosheets. *Appl. Surf. Sci.* **2021**, *535*, 147697. [CrossRef]
18. Yan, S.; Liang, X.; Song, H.; Ma, S.; Lu, Y. Synthesis of Porous CeO2-SnO2 Nanosheets Gas Sensors with Enhanced Sensitivity. *Ceram. Int.* **2018**, *44*, 358–363. [CrossRef]
19. Tan, C.; Cao, X.; Wu, X.-J.; He, Q.; Yang, J.; Zhang, X.; Chen, J.; Zhao, W.; Han, S.; Nam, G.-H.; et al. Recent Advances in Ultrathin Two-Dimensional Nanomaterials. *Chem. Rev.* **2017**, *117*, 6225–6331. [CrossRef] [PubMed]
20. Khatko, V.; Gorokh, G.; Mozalev, A.; Solovei, D.; Gispert Guirado, F.; Llobet, E.; Correig, X. Nanostructured Anodic Tungsten Oxide Films as a Promising Material For Gas Sensor Application. In Proceedings of the 20th European Conference on Solid State Transducers, EUROSENSORS XX, Goteborg, Sweden, 17–20 September 2006; Volume 2, pp. 332–333.
21. Karthikeyan, S.; Pandya, H.M.; Sharma, M.U.; Gopal, K. Gas Sensors—A Review. *J. Environ. Nanotechnol.* **2015**, *4*, 1–14. [CrossRef]
22. Fraden, J. *Handbook of Modern Sensors: Physics, Designs, and Applications*, 3rd ed.; Springer: New York, NY, USA, 2014; p. 589. ISBN 0-387-00750-4.

23. Wang, H.; Liu, X.; Niu, P.; Wang, S.; Shi, J.; Li, L. Porous Two-Dimensional Materials for Photocatalytic and Electrocatalytic Applications. *Matter* **2020**, *2*, 1377–1413. [CrossRef]
24. Neri, G. Thin 2D: The New Dimensionality in Gas Sensing. *Chemosensors* **2017**, *5*, 21. [CrossRef]
25. Chen, Y.; Li, H.; Huang, D.; Wang, X.; Wang, Y.; Wang, W.; Yi, M.; Cheng, Q.; Song, Y.; Han, G. Highly Sensitive and Selective Acetone Gas Sensors Based on Modified ZnO Nanomaterials. *Mater. Sci. Semicond. Process.* **2022**, *148*, 106807. [CrossRef]
26. Li, P.; Wang, B.; Wang, Y. Ultrafast CO Sensor Based on Flame-Annealed Porous CeO_2 Nanosheets for Environmental Application. *J. Inorg. Mater.* **2021**, *36*, 1223. [CrossRef]
27. Late, D.J.; Bhat, A.; Rout, C.S. *Fundamentals and Properties of 2D Materials in General and Sensing Applications*; Woodhead Publishing: Sawston, UK, 2019; pp. 5–24. [CrossRef]
28. Korotcenkov, G. The Role of Morphology and Crystallographic Structure of Metal Oxides in Response of Conductometric-Type Gas Sensors. *Mater. Sci. Eng. R Rep.* **2008**, *61*, 1–39. [CrossRef]
29. Younes, R.; Lakkis, S.; Alayli, Y.; Sawan, M. Review Of Recent Trends in Gas Sensing Technologies and Their Miniaturization Potential. *Sens. Rev.* **2014**, *34*, 24–35. [CrossRef]
30. Belahurov, E.A.; Khatko, V.V.; Gorokh, G.G.; Zakhlebayeva, A.I.; Reutskaya, O.G.; Taratyn, I.A. Low-Power Gas Sensor on Nanostructured Dielectric Membrane. *Nano Microsyst. Technol.* **2015**, *6*, 34–42.
31. Hwang, W.-J.; Shin, K.-S.; Roh, J.-H.; Lee, D.-S.; Choa, S.-H. Development of Micro-Heaters with Optimized Temperature Compensation Design for Gas Sensors. *Sensors* **2011**, *11*, 2580–2591. [CrossRef]
32. Calavia, R.; Mozalev, A.; Kahtko, V.; Gorokh, G.; Vilanova, X.; Correig, X.; Gracia, I.; Cané, C.; Llobet, E. A H2 Microsensor Based on Nanocolumnar Tungsten Oxide Grown by Template-Assisted Anodization. In Proceedings of the TRANSDUCERS 2009—15th International Conference on Solid-State Sensors, Actuators and Microsystems, Denver, CO, USA, 21–25 June 2009. [CrossRef]
33. Korotcenkov, G. Electrospun Metal Oxide Nanofibers and Their Conductometric Gas Sensor Application. Part 2: Gas Sensors and Their Advantages and Limitations. *Nanomaterials* **2021**, *11*, 1555. [CrossRef]
34. Dey, A. Semiconductor Metal Oxide Gas Sensors: A Review. *Mater. Sci. Eng. B Solid-State Mater. Adv. Technol.* **2018**, *229*, 206–217. [CrossRef]
35. Yang, S.; Jiang, C.; Wei, S.-H. Gas Sensing in 2D Materials. *Appl. Phys. Rev.* **2017**, *4*, 021304. [CrossRef]
36. Gorokh, G.G.; Zakhlebayeva, A.I.; Belahurau, Y.e.A.; Khatko, V.V.; Taratyn, I.A. Chemical gas sensors on the nanoporous anodic alumina substrate. *J. Nano-Microsyst. Techniq.* **2014**, *9*, 45–51.
37. Vasiliev, A.A.; Gogish-Klushin, S.Y.; Kharitonov, D.Y.; Pevgov, V.G.; Pislyakov, A.V. A new approach to micromachining technology for manufacturing sensors: Microelectronic chips with a thin aluminum oxide membrane. *Sensor* **2002**, *3*, 23–29. (In Russian)
38. Kalinin, I.A.; Roslyakov, I.V.; Tsymbarenko, D.M.; Bograchev, D.A.; Krivetskiy, V.V.; Napolskii, K.S. Microhotplates based on Pt and Pt-Rh films: The impact of composition, structure, and thermal treatment on functional properties. *Sens. Actuators A Phys.* **2021**, *317*, 112457. [CrossRef]
39. Vasiliev, A.A.; Pisliakov, A.V.; Sokolov, A.V.; Samotaev, N.N.; Soloviev, S.A.; Oblov, K.; Guarnieri, V.; Lorenzelli, L.; Brunelli, J.; Maglione, A.; et al. Non-Silicon MEMS Platforms for Gas Sensors. *Sens. Actuators B Chem.* **2016**, *224*, 700–713. [CrossRef]
40. Moon, S.E.; Choi, N.-J.; Lee, H.-K.; Lee, J.; Yang, W.S. Semiconductor-Type MEMS Gas Sensor for Real-Time Environmental Monitoring Applications. *ETRI J.* **2013**, *35*, 617–624. [CrossRef]
41. Xia, Z.; Riester, L.; Sheldon, B.; Curtin, W.; Liang, J.; Yin, A.; Xu, J. Mechanical Properties of Highly Ordered Nanoporous Anodic Alumina Membranes. *Adv. Mater. Sci.* **2004**, *6*, 131–139.
42. Gorokh, G.; Pashechko, M.I.; Borc, J.; Lazavenka, A.; Kashko, I.A.; Latos, A.I. Matrix Coatings Based on Anodic Alumina with Carbon Nanostructures in the Pores. *Appl. Surf. Sci.* **2017**, *433*, 829–835. [CrossRef]
43. Zakhlebayeva, A.; Lazavenka, A.; Gorokh, G. Multicomponent Sn–Mo–O-Containing Films Formed in Anodic Alumina Matrixes by Ionic Layer Deposition. *Mater. Today Proc.* **2021**, *37*, 4064–4070. [CrossRef]
44. Lee, S.M.; Dyer, D.C.; Gardner, J.W. Design and Optimisation of a High-Temperature Silicon Micro-Hotplate for Nanoporous Palladium Pellistors. *Microelectron. J.* **2003**, *34*, 115–126. [CrossRef]
45. Gorokh, G.; Bogomazova, N.; Taleb, A.; Zhylinski, V.; Galkovsky, T.; Zakhlebayeva, A.; Lozovenko, A.; Iji, M.; Fedosenko, V.; Tolstoy, V. Spatially Ordered Matrix of Nanostructured Tin–Tungsten Oxides Nanocomposites Formed by Ionic Layer Deposition for Gas Sensing. *Sensors* **2021**, *21*, 4169. [CrossRef]
46. Gorokh, G.; Zakhlebayeva, A.; Taratyn, I.; Lozovenko, A.; Zhylinski, V.; Iji, M.; Fedosenko, V.; Taleb, A. A Micropowered Chemoresistive Sensor Based on a Thin Alumina Nanoporous Membrane and SnxBikMoyOz Nanocomposite. *Sensors* **2022**, *22*, 3640. [CrossRef]
47. Manikandan, V.; Vigneselvan, S.; Petrila, I.; Mane, R.S.; Singh, A.; Sobczak, K.; Chandrasekaran, J. Long-lasting stability and low-concentration SO_2 gas detection aptitude of Sn-doped alumina sensors. *Mater. Chem. Phys.* **2022**, *291*, 126691. [CrossRef]